Effects of embedding depth and load eccentricity on lateral response of offshore monopiles in dense sand: A centrifuge study

Zhongsen Li, Matthieu Blanc, Luc Thorel

Li, Zhongsen; Blanc, Matthieu; Thorel, Luc

Effects of embedding depth and load eccentricity on lateral response of offshore monopiles in dense sand: A centrifuge study

Published in:

Géotechnique

DOI:

10.1680/jgeot.21.00200

Published: 13/12/2021

Document Version

Peer reviewed version

Please cite the original version: Li, Z., Blanc, M., & Thorel, L. (2021). Effects of embedding depth and load eccentricity on lateral response of offshore monopiles in dense sand: A centrifuge study, *Géotechnique*. https://doi.org/10.1680/jgeot.21.00200

Effects of embedding depth and load eccentricity on lateral response of offshore monopiles in dense sand: A centrifuge study

Zhong-Sen LI

Post-doctoral researcher; Laboratory of Geomaterials and Modelling in Geotechnics, Department GERS, University Gustave Eiffel, Bouguenais, France (currently at Department of Civil Engineering, Aalto University, Otaniemi, Finland); ORCID: 0000-0002-3380-4000

Matthieu BLANC (corresponding author)

Researcher; Laboratory of Geomaterials and Modelling in Geotechnics, Department GERS, University Gustave Eiffel, Bouguenais, France; ORCID: 0000-0003-0603-487X; Contact: matthieu.blanc@univ-eiffel.fr, +33 2 40 84 58 18

Luc THOREL

Senior Researcher; Laboratory of Geomaterials and Modelling in Geotechnics, Department GERS, University Gustave Eiffel, Bouguenais, France; ORCID: 0000-0002-0218-4144

Manuscript finished on June 9th, 2020
Manuscript revised on July 12th, 2021
Number of words in the main text: 5107
Number of figures: 16
Number of tables: 2

Abstract: Two model piles with outer diameter D = 50 mm are loaded laterally at 100×g in a large-beam geotechnical centrifuge. The normal strains on both the tensile and compressive sides are measured using fibre Bragg gratings. An incremental method is introduced to define the pivot point. The testing and analytical program enables the effect of the embedding depth and load eccentricity to be quantified. The key findings are as follows. 1) The piles generate asymmetric tensile and compressive strains during bending, and the tension-compression asymmetry becomes more pronounced at the pile toe and for shorter piles. 2) The piles transition from flexure to rotation as the embedding depth is decreased from 9D to 3D, where the uniqueness of the ground-level rotation and deflection (θ_g–y_g) relationship disappears. 3) The reaction and deflection (P–y) relationship flattens with increasing embedding depth but seems independent of the load eccentricity.

Keywords: Monopile; Lateral response; Embedding depth; Eccentricity; Sand

List of notations:

D	Outer diameter of the pile (m)
d	Inner diameter of the pile (m)
E	Young's modulus (Pa)
g	Gravitational acceleration (m/s^2)
M	Bending moment (N·m)
H	Applied lateral load (N)
H_g	Lateral load at ground level (N)
i, j	Iterative parameter
I	Moment of inertia of an area (m^4)
L_e	Load eccentricity (m)
L	Embedding depth of the pile (m)
L_t	Wall thickness of the pile (m)
M_g	Bending moment at ground level (N·m)
P	Soil reaction (kN/m)
ε_T	Tensile strain
ε_C	Compressive strain
S	Distance between the pile centre to the container wall (m)
θ_g	Rotation angle at ground level (°)
y	Lateral deflection (m)
y_g	Lateral deflection at ground level (m)
z	Depth of the FBGs or soil (m)
z_{Pivot}	Depth of the pivot point (m)

1. Introduction

A joint academia-industry project, SOLCYP (the French acronym for CYclic SOLicitations on Piles), was initiated in 2008 with the aim of improving the design methodologies for axially and laterally loaded piles (Puech *et al.*, 2012). Its extension SOLCYP+ was launched recently and is focused on the lateral responses of monopile foundations for offshore wind turbines (FEM, 2019). As part of the SOLCYP+ project, the present study is aimed at enriching the database of laterally loaded monopiles.

Under lateral loads, monopiles undergo both bending and rotation, the ratio of which depends on the embedding depth and rigidity. In general, short embedded piles tend to rotate around a pivot point without significant bending, whereas slender and deeply embedded piles mainly bend with little rotation. Because pile behaviour transitions with changing embedding depth, it is highly recommended to develop specific design codes for short and large-diameter monopiles, which are now the major supporting structures for offshore wind turbines (Puech & Garnier, 2017).

In the framework of recent joint academia-industry projects, such as PISA (Pile Soil Analysis; Byrne *et al.*, 2017) and ALPACA (Axial-Lateral Pile Analysis for Chalk Applying multi-scale field and laboratory testing; Jardine *et al.*, 2019), large-scale field tests were performed on monopiles in sand, clay and chalk sites. The results were advantageous in that the site conditions and stress levels were close to those in engineering practice, but at the cost of high budgets and being under partial saturation (e.g. PISA). For these reasons, only a few tests were reported in the past decade and the experimental data are scarce. As an alternative, physical modelling by geotechnical centrifuge seems promising to fill the gap because it allows parametric studies to be performed conveniently while also providing a stress field that is comparable to that under field conditions.

In the literature, tests are being performed increasingly at major centrifuge centres to investigate the lateral responses of monopiles (e.g. Georgiadis *et al.*, 1992; Li *et al.*, 2010; Klinkvort & Hededal, 2014; Bayton & Black, 2016; Choo & Kim, 2016; Darvishi Alamouti *et al.*, 2019; Truong *et al.*, 2019; Kong *et al.*, 2021). At the centrifuge centre of Gustave Eiffel University (formerly known as IFSTTAR or LCPC), lateral loading tests have been conducted continuously in several doctoral projects (Mezazigh, 1995; Remaud 1999; Rosquoët, 2004; Rosquoët *et al.*, 2007; Rakotonindriana, 2009; El Haffar *et al.*, 2017,

2020; El Haffar, 2018). However, in all those studies, strain gauges were glued onto the outer or inner side of the piles, the dimensions and surface condition of which were altered because of the gauge coating and associated cables. Also, the model piles were mostly installed in dry sand, which is not the case in offshore sites.

To make progress, the quality and representativeness of the tests were improved in present study by (i) using optical fibres to work on open-ended model piles while not affecting the wall thickness, (ii) double checking the calculations with a new analytical method and iii) scaling up the dimensions of the model piles to take full advantage of the maximum bearing capacity (i.e. 2 tons) of the large-beam centrifuge.

2. Materials and experimental methods

Two circular aluminium piles with an outer diameter of 50 mm and a wall thickness of 2.5 mm were used. At 975-mm long, pile 1 was 50 mm shorter than pile 2. The mechanical properties of the two piles were identical, with a Young's modulus of 74 GPa and an elastic limit of 248 MPa. In the laboratory, the piles were instrumented with optical fibres, within which a couple of fibre Bragg gratings (FBGs) had been integrated. Pile 1 had a span of 425 mm for 13 FBGs, whereas pile 2 had a span of 225 mm with 10 FBGs distributed equally. The instrumented piles are shown photographically and schematically in Figure 1. Further details about the instrumentation and calibration methods can be found in Li *et al.* (2020).

The soil specimens were prepared with an automatic raining technique (Garnier, 2001). Dry Fontainebleau NE34 sand (Table 1) was first sucked into a feed hopper located on top of a strongbox, the dimensions of which were 1200 mm (length) by 800 mm (width) by 720 mm (height). The sand was then pluviated into the strongbox through a 3-mm-wide slit. During the raining process, the hopper moved back and forth at a constant speed of 100 mm/s, while keeping a constant height from the sand surface by means of a laser ranging and adaptive control system. When the sand height reached at 600 mm, the hopper stopped feeding. The sand in the upper layer, normally with a lower density and a concave surface, was removed by means of a vacuum cleaner. The protocol enabled homogeneous 1200 mm by 800 mm by 560 mm sand specimens to be obtained. The resulting density was 1.677 g/cm^3, i.e. 81% in relative density by knowing the minimum and maximum dry densities (Table 1). The

dry specimens were saturated by inputting water through four channels at the bottom of the strongbox. The water head was kept at ~20 cm so that the water infiltration didn't disturb the sand specimens. The saturation terminated when the water level reached at 30 mm above the sand surface, and the saturated density was 2.043 g/cm^3.

The instrumented model piles were pushed into the sand at 1×*g* level by a hydraulic jack. The jacking speed was 1 mm/s and the attained depths were 150, 250, 350 and 450 mm. The sand elevation inside the pile was checked. Unlike in the in-situ cases (e.g. driving at *N*×*g* or in the field), no sand plug was observed in present study. Having installed the piles, the strongbox was moved into the basket of the centrifuge. Supporting beams were placed and fixed onto the longitudinal edges of the strongbox. An electric actuator, a load cell, two cameras and four laser sensors were mounted on the supporting beams. The established testing system is shown in Figure 2.

Prior to the lateral loading, the relative centrifugal force in the strongbox was elevated progressively and then maintained at 100×*g* for half an hour, during which time the water level, verticality of the pile and the readings of the FBGs, load cell and laser sensors were checked. Then, a lateral load was applied through the electric actuator by pushing a steel rod that crossed the model piles diametrically. The test was conducted in the displacement-control mode to define the back-bone curves, even though the stress-control mode is more typical in practice. The loading rate was 0.1 mm/s at the actuator level. The measurements of the FBGs, load cell and lasers were recorded and saved at 50 Hz. The test terminated when the calculated deflection at the ground reached ~5 mm (0.1D). Compared to the service condition (typically 0.25° in rotation), the piles were overloaded to ground-level rotations of 1.8–4.0°.

Seven tests were performed in two strong boxes. In tests 1–4, the load eccentricity was 500 mm (i.e. 10*D*) and the embedding depths were 250, 350, 450 and 150 mm (i.e. 5*D*, 7*D*, 9*D* and 3*D*), respectively. In tests 1, 5 and 6, the load eccentricities were 500, 750 and 250 mm (i.e. 10*D*, 15*D* and 5*D*), respectively, while the embedding depths were the same, i.e. 250 mm (5*D*). Test 7, performed in the next strongbox, was a repeat of test 1 because one of the optical fibres lost the connection with the interrogator. The testing program is shown schematically in Figure 3.

The effect of the side boundary of the container was checked with centrifuge cone-penetration tests also on Fontainebleau sand (Bolton *et al.*, 1999). In tests 1 and 2, the normalised distance to the container wall (*S*/*D*) was 6, which added ~5% extra resistance in comparison with *S*/*D* ratios of larger than 10. The side-boundary effect was negligible in tests 3-7 with *S*/*D* ratios of 12 or 19. In present study, the model piles were installed and uninstalled repeatedly in the same strongbox. The spin-up during pile installation may have disturbed the adjacent sand bed, but this was found to be insignificant because the model piles were smooth enough, as evidenced by the absence of a plug during installation.

3. Analytical methods

By following the law of similitude, the parameters in the modelling tests were scaled up to those of the prototype (Table 2), based on which the other parameters are calculated and presented throughout this paper. Under lateral loading, the pile bends and generates normal strains that are either tensile or compressive. The strains below the ground were measured by the FBGs and then used to calculate the corresponding values of the bending moment *M* via the following equation:

$$M = \frac{EI(\varepsilon_T - \varepsilon_C)}{D} \quad (1)$$

where *E* [Pa] is the Young's modulus of the pile, *I* [m^4] is its moment of inertia, *D* [m] is its outer diameter and ε_T and ε_C are the measured tensile and compressive strains, respectively.

The calculated bending moment was segmented based on the value at ground level, e.g. every 100 MN·m for test 1. Along the pile embedding depth, the measured bending moments are discrete and must be smoothed. This was achieved by the cubic spline curve-fitting technique, which was proved better than the high degree polynomials for laterally loaded piles (Haiderali & Madabhushi, 2016). The smoothed moment profiles were used to determine (i) the shear force and soil reaction by conducting first and second order differential operations and (ii) the pile rotation angle and deflection by solving first- and second-order integrals, respectively. In the second definite integration of the bending moments, two integration constants were required. These were determined by solving a simultaneous equation with known boundary conditions, i.e. (i) the pile deflection measured by the electric actuator or the laser sensors and (ii) the pivot point based on the following analysis of the soil reaction:

- Global method. The assumptions of this routine method are that (i) the pile rotates at the depth at which the sign of the reaction changes and (ii) the pile deflection is equal to zero at the pivot point, i.e. $y(z_i) = 0$ when $P(z_i) = 0$. Thus, the method relies on finding the points at which the soil reaction is null and then assigning the corresponding pile deflection to be zero.
- Incremental method. The pile is supposed to rotate at the depth z_i whose soil reaction at the current load is equal to that at the previous load, i.e. $y^j(z_i) = y^{j-1}(z_i)$ when $P^j(z_i) = P^{j-1}(z_i)$. The method involves finding the first rotation point whose soil reaction is null, i.e. $P^1(z_i) = 0$, identifying the intersection of the j^{th} and $(j\text{-}1)^{th}$ reaction profiles, considering the point $(z_i, P^j(z_i))$ as the pivot point of the j^{th} load and assigning the corresponding deflection $y^j(z_i)$ equal to $y^{j-1}(z_i)$.

In summary, with the global method the pivot point is the intersection of the y-axis and reaction profile and the corresponding lateral displacement y is zero, whereas with the incremental method the pivot point is the intersection of two adjacent reaction profiles and the corresponding y is not zero. Figure 4 shows the principles and differences of the two methods. In present study, the incremental method was preferred, and the global method served as a reference to verify the applicability of the incremental method.

The above calculations give the profiles of the pile shear force, soil reaction and pile rotation and deflection. This allows analysis of both the local and global behaviour of the piles. The sequence of the data processing in current study is shown in Figure 5.

4. Results

4.1 Tests at constant load eccentricity (L_e/D = 10)

Four tests were performed with the same load eccentricity (i.e. L_e/D = 10). Local strains, measured by the FBGs, are first presented in Figure 6 for typical ground-level bending moments (i.e. every 50, 100 and 200 MN·m for the embedding depths of 3D, 5D and 7D, respectively). As the normalised embedding depth L/D is decreased from 9 to 3, the tensile strains at the pile toe increase significantly, whereas the compressive strains change less prominently. At a given depth, the tensile and compressive strains are asymmetric, especially at the pile toe and for shorter piles. The observed tension-compression asymmetry is checked and repeatedly observed even with a new model pile (D = 100 mm) that

instrumented with another set of FBGs. Similar observations were also noticed in field tests on University College Dublin dense sand (Doherty *et al.*, 2015) and Dunkirk marine dense sand (McAdam *et al.*, 2020). In the former case, the authors suggested the shift in neutral axis towards the compressive side as the reason for the smaller compressive strains, whereas in the latter case the large tension-compression asymmetry was considered unusual but not explained. In Figure 6b, the difference between the tensile and compressive strains is quantified. Above ground level, the tensile strains are larger than the compressive ones and the differential strains are positive. This can be explained by the shift of the neutral axis (Doherty *et al.*, 2015). In the superficial layer below the ground, the pile deflection induces constraints from the soil (negative earth pressure) that in return prevent the pile from advancing. The large constrains on the pile front enhance the soil-pile contact and increase the tangential and friction stresses. Consequently, the strains on the pile front (i.e. compressive strains) increase and may become larger than the tensile strains, such as for L/D = 3 and 5. In the deep layer below the ground, the tensile strains are always larger than the compressive one; this is due to the combined effects of larger (i) constraints (negative earth pressure or soil reaction), (ii) shaft friction and (iii) base shear on the negative mobilisation zone.

Figure 7 (from left to right) presents the profiles of pile deflection, rotation angle, bending moment, shear force and soil reaction. As a general feature, the ground-level bending moments calculated from the strains (i.e. the cross symbols) are consistent with those calculated from the applied force, as are the ground-level shear forces. At the pile toe, as L/D is increased from 3 to 9, the deflection and rotation angle decrease to null even though the applied bending moments are larger. At L/D = 3, the profiles of the pile deflection can be deemed as a series of straight lines, meaning that the pile only rotates and there is practically no flexure. At L/D = 9, the deflection at depths of 7–9D is almost null, indicating a strong embedding force and negligible rotation. For the values of L/D in between, one may notice a series of curved lines with nonzero values at the pile end, which in fact suggest a combination of rotation and flexure. In the present study, the pile behaviour undergoes a clear transition (i.e. from rigid rotation to pure flexure) as the generalised embedding depth L/D is increased from 3 to 9. This agrees well with the field results of Shakhirev & Ejjaouani (1995) and McAdam et al. (2020).

Based on the profile of the soil reaction, the pivot points were determined with the incremental and global methods. In Figure 8, the normalised depth of the pivot points z_{Pivot}/L is plotted versus the normalised ground-level deflection y_g/D. For the L/D ratio of 5, 7 and 9, the pivot depth moves

downwards and tends to stabilise when the lateral deflection exceeds 0.1D. The results are consistent with those from previous field tests (e.g. Shakhirev & Ejjaouani, 1995; McAdam *et al.*, 2020; Byrne *et al.*, 2020), showing that as the applied lateral force increases, the soil resistance in the upper layers is exhausted as a result of the development of plastic deformations, and the soil layers located below are put to work to maintain the pile in static equilibrium. For the short pile (L/D = 3), the pivot depth changes oppositely with the lateral deflection. In the initial stage of lateral loading, the depth of the pivot point is 0.83L or 0.81L, which is much deeper than the previous ones. The shift of the initial pivot point towards the pile toe is probably a result of the increasing relative self-weight of the pile above the ground and the diminishing lateral constraints and friction. At L/D = 3, the ratio of the self-weight to the friction or lateral constraints is much larger than those of the longer piles. The increasing relative vertical force causes the initial pivot point to move downwards, as evidenced by the field results of Shakhirev & Ejjaouani (1995). Both the incremental and global methods capture the general trend of the curve of z_{Pivot}/L versus y_g/D. In general, the incremental method yields a larger and unified value for z_{Pivot}/L (i.e. 0.7) as the deflection reaches 0.1D, whereas with the global method the stabilised z_{Pivot}/L decreases from 0.79 to 0.6 when L/D is increased from 5 to 9. The latter seems more consistent with the recent field tests at Dunkirk, where McAdam *et al.* (2020) found that the value of z_{Pivot}/L decreased from 0.74 to 0.61 as L/D was increased from 3 to 8.

Figure 9 shows the relationship between the soil reaction P and the normalised deflection y/D at different depths. Also presented are the corresponding curves based on the standard (DNV-GL, 2017) and the literature (Georgiadis *et al.*, 1992). As a common feature, the slope of the P–y/D curve increases with increasing depth. This is expected and reasonable because the soil is stiffer in the deeper layer. For a given depth (z = 0.5D), the P–y/D curve tends to be steeper when the slenderness ratio is decreased from 9 to 3. This seems unusual given that the soil stiffness is constant and its stress–strain relationship should be unique at that depth. One possible reason of the steepening P–y/D curve is that Euler-Bernoulli beam theory underestimates the lateral deflection of short piles. At L/D = 9, the correlation of Georgiadis *et al.* (1992) captures well the initial stiffness and continuous-hardening phenomenon of the soil, whereas DNV-GL (2017) yields significantly larger initial soil stiffness. The latter was highlighted by Choo & Kim (2016), Darvishi Alamouti *et al.* (2019), Zhu *et al.* (2019) and Lee *et al.* (2019). At L/D = 3, the experimental P–y/D curve deviates from the reference of Georgiadis *et al.* (1992) and approaches the correlation of DNV-GL (2017). The latter correspondence seems to be a

coincidence. Nevertheless, one should be cautious when comparing the results from centrifuge tests with those from field tests or standards (e.g. API, 2010; DNV-GL, 2017) because the sand is completely disturbed during pluviation in centrifuge tests, whereas it has more complex bonds in the field because of the effects of aging (Remaud, 1999; Schmertmann, 1991; Mitchell, 2008) and suction. In addition, the difference in pile-installation gravity (1×*g* or N×*g*) can result in apparent increases in measured stiffnesses by a factor of 1.52 when N = 100 (Fan et al., 2021). Other factors such as the lateral loading rate have been found to affect the initial stiffness as well (Beuckelaers, 2017; El Haffar, 2018). Below the pivot point, the soil reaction becomes negative because of the increasing constraints on the back side of the pile. The slope of the *P*–*y*/*D* curve becomes linear at depths close to the toe (e.g. 7*D*) for *L*/*D* = 9 and becomes as large as 1100 MN/m, which is about five times that for *L*/*D* = 3 at the depth of 2*D*.

In Figure 10, the ground-level bending moment M_g and lateral load H_g are plotted versus the corresponding normalised lateral deflection y_g/D and rotation θ_g. The empty symbols represent the parameters derived from the FBGs measurements, whereas the solid symbols are those from the actuator. As with the comparisons in Figure 7, the FBGs and actuator yield satisfactory agreements in terms of the ground-level moments and forces. Under a given bending moment M_g or load H_g, the resulting ground-level deflection y_g/D or rotation θ_g decreases with increasing embedding depth, confirming that deeper embedment can better resist the overturning moments and force. However, this effect becomes negligible when *L*/*D* shifts from 7 to 9. The relationship between the normalised deflection y_g/D and rotation θ_g is linear and unique for *L*/*D* of 5, 7, and 9. For *L*/*D* = 3, however, more rotation is generated under the same lateral deflection. Further inspection of the results implies that (i) there is a uniqueness between M_g–y_g (or M_g–θ_g, H_g–y_g, H_g–θ_g) when $L/D \geq 7$ and (ii) the uniqueness between y_g–θ_g disappears when $L/D < 5$.

4.2 Tests at constant embedding depth (*L*/*D* = 5)

The compressive and tensile strains are presented in Figure 11 for ground-level moments of 100, 200, 300, 400 and 500 MN·m. The three tests give coherent results except that the third FBG (highlighted with the rectangular box) worked less correctly. With decreasing load eccentricity, the strain profile becomes wider; the mechanism for this is unclear and worth studying further. In the upper part of the

pile (i.e. 1.0–2.5D), the compressive strains are larger than the tensile ones because of the larger constraints on the front side, i.e. negative earth pressure. At greater depths, the situation reverses, and the asymmetry becomes more significant because of the shifts of the negative mobilisation zone from front to back (as in Figure 6).

In Figure 12, the corresponding bending moments are presented, followed by the plots of the deflection, rotation, shear force and soil reaction versus the normalised depth for load eccentricity L_e of 5D, 10D and 15D. Similar to Figure 7, the measurements of FBGs and actuator are consistent in terms of the ground-level moments and shear forces. With increasing L_e, the depth corresponding to the maximum bending moment decreases from 1.5–1D, and the pile rotation and deflection become less. Nevertheless, the pivot depth seems to be independent of the load eccentricity, as can be seen in Figure 13. With the incremental method, the stabilised pivot depth is ~0.75L, which is slightly smaller than that with the global method, i.e. 0.8L.

Figure 14 shows the normalised P–y/D plots. Each series of the same symbols (e.g. circles, squares) represent the evolution of the pile–soil interaction at the same depth (e.g. 0.5D, 1D). Even though larger deflection and reaction have been generated, the P–y/D relationships of the L_e = 5D are practically the same as those with L_e of 10D and 15D in terms of the slope, showing that the load eccentricity has negligible impact on the initial stiffness. However, this is not the case for the ground-level deflection and rotation. As shown in Figure 15, under a given ground-level bending moments or lateral force, the pile with smaller load eccentricity gains more deflection or rotation, suggesting that in practice currents and waves below sea level will result in more deflection and rotation than will the winds above sea level. For these three tests, there is a linear and unique relationship between the ground-level rotation and deflection.

5. Discussion

The present measurement and analytical methods reveal two striking phenomena for laterally loaded monopiles: (i) tension-compression asymmetry and ii) pivot point shift. These phenomena especially the first one have not been reported well in the literature and so are discussed in more details herein.

5.1 Dependence of tension-compression asymmetry on embedding depth

The use of FBGs shows advantages in limiting the impacts of the geometry and smoothness of the model pile associated with traditional strain gauging. As measured by FBGs, the tensile and compressive strains are asymmetric at a given cross section. The degree of the tension-compression asymmetry changes with the pile embedding depth (Figures 6 and 11) and appears to be related to the following factors.

- Strength differential effect. Aluminium alloys normally exhibit smaller strength in tension than in compression (Holmen et al., 2017). The Young's modulus is slightly larger in compression than in tension ($E_C > E_T$); therefore, the tensile strains are larger than the compressive for the pile under pure bending. This leads the neutral axis to shift towards the intrados, as observed by Doherty *et al.* (2015).
- Shaft friction. As the pile rotates or flexes in the sand bed, the soil reaction is much larger in the passive mobilisation zone than in the positive zone, as is the shaft friction. The larger shaft friction results in larger normal strains in the passive zone than in the positive zone.
- Base shear. The base shear of monopiles is large because of the significant lateral displacement of the pile toe (e.g. L/D = 3 in Figures 6 and 7). The base shear adds extra bending moment at the pile toe and enhances the soil-pile contact and the shaft friction; therefore, the normal strains are large on one side (i.e. the passive mobilisation zone) of the pile toe.
- Base resistance. The base resistance resists the rotation of the pile. It is larger in the positive mobilisation zone than in the passive zone; therefore, larger normal strains are expected on the positive side with the effect of the base resistance.

Figure 16 illustrates the afore-mentioned constraints from the soil bed. The dependence of the tension-compression asymmetry on the pile embedding depth can be explained qualitatively as follows.

- Above ground. There is no soil surrounding the pile. The observed larger tensile strains are mainly attributed to the smaller tensile Young's modulus. Besides, the axial component of the applied lateral load contributes also to the larger tensile strains.
- Below ground but above a certain depth (near the pivot point). The passive mobilisation zone is located in the front, and the shaft friction is larger on the front surface of the pile than on the back. The asymmetric shaft friction increases with increasing embedding depth and counteracts the

strength differential effect. Consequently, the compressive strains become larger than the compressive ones after a certain depth.

- Below the pivot point. The passive mobilisation zone moves from front to back. The tension-compression strength difference, shaft friction and base shear favour the larger tensile strains at the pile back, whereas the base resistance favours the larger compressive strains at the front. Because the effect of base resistance alone is less significant than the others, the net strains are tensile.

5.2 Criteria for identifying pivot points

The pivot points are identified with two analytical methods, designated as global and incremental methods. The criteria for identifying the pivot points are 'P = 0' and 'ΔP = 0', respectively. The pivot points determined by the global and incremental methods share similar trend in terms of the pivot depth versus lateral displacement. The advantage of using the incremental method is insignificant in present study because of the nature of the lateral loading, which is monotonic and sufficiently small. It would be interesting to compare both methods in cyclic tests because P = 0 is no longer a sign of y = 0 during unloading, and the traditional global method appears to be erroneous.

The centrifuge results for piles with embedding depths of 5D, 7D and 9D confirm previous observations that the normalised pivot depth (i.e. z_{Pivot}/L) tends to stabilise at 0.7±0.1 (Zhang et al., 2021). However, the pile with an embedding depth of 3D behaves differently and the normalised pivot depth is ~0.55.

5.3 Limitations and suggestions

In present study, the ratio of the wall thickness to grain size (L_t/d_{50}) was 11.9 and ~100 times smaller than that in practice. It is unclear whether this reduced L_t/d_{50} ratio affected the base resistance (i.e. tip pressure) or not because no comparison could be found in the literature. Also, there would have been a scale effect related to the roughness because the model aluminium piles were smoother than offshore steel monopiles.

The interpretation of the tension-compression asymmetry remains qualitative and somewhat speculative in present study. Further investigations are needed to verify the dependence of the tension-compression asymmetry on loading mode (monotonic or cyclic), soil condition (dense or loose) and installation mode (1×g or N×g). Suggestions for future relevant studies include (i) instrumenting the

strain gauges or FBGs more densely at the pile toe to better capture the large shear force there and (ii) using tactile pressure sensors (Palmer et al., 2009) to measure the soil–pile contact pressure directly.

6. Conclusion

Monopiles were subjected to lateral monotonic loading in a geotechnical centrifuge with embedding depth or load eccentricity controlled. The common findings are as follows:

- The compressive and tensile strains are asymmetric. Above the ground, tensile strains are more significant as the neutral axis moves towards the compressive side due to the strength differential and/or scale effects. At shallow depths below the ground, larger constraints (i.e., negative earth pressure) are generated on the pile's front where compressive strains start to overcome the effect of the non-centred neutral axis and become larger than the tensile strains. At greater depths, the region of negative earth pressure moves to the back of the pile. Tensile strains become dominant because of the combined effects of larger constrains, friction and base shear on the negative mobilisation zone.
- The FBGs work properly at 100×*g* level. The ground-level bending moments and shear force, calculated from the measurements of the FBGs, are coherent with those calculated from the actuator force.
- The incremental method is shown to be useful and reliable for determining the pivot point.

Specifically, the tests with constant load eccentricity show the following:

- The tension-compression asymmetry is more important at the pile toe and for shorter piles.
- The pile behaviour transitions from rigid rotation to pure flexure when the normalised embedding depth L/D is increased from 3 to 9.
- The pivot point moves upwards for the short pile (i.e. L/D = 3) but downwards for long piles when the lateral load increases.
- The P–y curves flatten with increasing normalised embedding depth. The parabolic correlations in Georgiadis et al. (1992) capture well the initial stiffness and continuous-hardening feature, but only for the longer pile (i.e. L/D = 9).
- There is a uniqueness between M_g–y_g (or M_g–θ_g, H_g–y_g, H_g–θ_g) for L /D ≥ 7.

- The uniqueness between y_g–θ_g disappears when L/D changes from 5 to 3.

The tests at constant embedding depth show the following:

- The profiles of the strains and bending moments become wider with decreasing load eccentricity, which yields larger pile deflection and rotation for a given ground-level force or moment. This suggests that in practice monopile foundations are more sensitive to the loads of currents and waves than to wind loading.
- The P–y curve, pivot depth and y_g–θ_g relationship are independent of the load eccentricity.

Acknowledgement
This work received state support managed by the National Research Agency under the Investments for the Future Program (ANR-10-IEED-0006-08) and financial support from France Energies Marines (SOLCYP+). The technical staff at the centrifuge group of Gustave Eiffel University helped in building up the experimental devices.

Data availability statement
The data presented in this study are available from the first author upon request.

Reference

API (2010). RP 1A-WSD - recommended practice for planning, designing and constructing fixed offshore platforms. Washington: American Petroleum Institute.

Bayton, S. M. & Black, J. A. (2016). The effect of soil density on offshore wind turbine monopile foundation performance. Proc. 3rd European Conf. on Physical Modelling in Geotechnics, Nantes, 239-244.

Beuckelaers, W. (2017). Numerical modelling of laterally loaded piles for offshore wind turbines. Doctoral dissertation, University of Oxford, Oxford, UK.

Bolton, M. D., Gui, M. W., Garnier, J., Corte, J. F., Bagge, G., Laue, J. & Renzi, R. (1999). Centrifuge cone penetration tests in sand. Géotechnique **49**, No. 4, 543-552.

Byrne, B. W., McAdam, R. A., Burd, H. J., Beuckelaers, W. J. A. P., Gavin, K. G., Houlsby, G. T., Igoe, D. J. P., Jardine, R. J., Martin, C. M., Muir Wood, A., Potts, D. M., Skov Gretlund, J., Taborda, D. M. G. & Zdravković, L. (2020). Monotonic laterally loaded pile testing in a stiff glacial clay till at Cowden. Géotechnique **70**, No. 11, 970-985.

Byrne, B. W., McAdam, R. A., Burd, H. J., Houlsby, G. T., Martin, C. M., Beuckelaers, W. J. A. P., Zdravković, L., Taborda, D. M. G., Potts, D. M., Jardine, R. J., Ushev, E., Liu, T., Abadias D., Gavin, K. G., Igoe, D., Doherty, P., Skov Gretlund, J., Pacheco Andrade, M., Muir Wood, A., Schroeder, F. C., Turner, S. & Plummer M. A. L., 2017. PISA: New design methods for offshore wind turbine monopiles. Proc. 8th Int. Conf. on Offshore Site Investigation and Geotechnics, London, Vol 1, 142-161.

Choo, Y. W. & Kim, D. (2016). Experimental development of the p-y relationship for large-diameter offshore monopiles in sands: Centrifuge tests. Journal of Geotechnical and Geoenvironmental Engineering **142**, No. 1, 04015058.

Darvishi Alamouti, S., Moradi, M. & Bahaari, M. R. (2019). Centrifuge modelling of monopiles subjected to lateral loading. Scientia Iranica **26**, No. 6, 3109-3124.

DNV-GL. (2017). Offshore soil mechanics and geotechnical engineering. Offshore Standard DNVGL-RP-C212, Oslo, Det Norske Veritas and Germanischer Lloyd.

Doherty, P., Igoe, D., Murphy, G., Gavin, K. G., Preston, J., McAvoy, C., Byrne, B. W., McAdam, R., Burd, H. J., Houlsby, G. T., Martin, C. M., Zdravković, L., Taborda, D. M. G., Potts, D. M., Jardine, R. J., Sideri, M., Schroeder, F. C., Muir Wood, A., Kallehave, D. & Skov Gretlund, J. (2015). Field validation of fibre Bragg grating sensors for measuring strain on driven steel piles. Géotechnique Letters **5**, No. 2, 74–79.

El Haffar, I., Blanc, M. & Thorel, L. (2017). Impact of pile installation method on the axial capacity in sand. Géotechnique Letters **7**, No. 3, 260-265.

El Haffar, I. (2018). Physical modelling and study of the behaviour of deep foundations of offshore wind turbines in sand. Doctoral dissertation, École Centrale de Nantes, Nantes, France (in French).

El Haffar, I., Blanc, M. & Thorel, L. (2020). Impact of pile roughness on shaft resistance in sand. Proceedings of the Institution of Civil Engineers - Geotechnical Engineering **173**, No. 1, 81-91.

Fan, S., Bienen, B. & Randolph, M. F. (2021). Centrifuge study on effect of installation method on lateral response of monopiles in sand. International Journal of Physical Modelling in Geotechnics, **21**, No. 1, 40-52.

France Energies Marines (2019) https://en.france-energies-marines.org/R-D/Projects-in-progress/SOLCYP (Accessed on May 14th, 2020).

Garnier, J. (2001). Modèles physiques en géotechnique I - Évolution des techniques expérimentales et des domaines d'application. Revue Française de Géotechnique, No. 97, 3-29.

Georgiadis, M., Anagnostopoulos, C. & Saflekou, S. (1992). Centrifugal testing of laterally loaded piles in sand. Canadian Geotechnical Journal **29**, No. 2, 208-216.

Haiderali, A. E. & Madabhushi, G. (2016). Evaluation of curve fitting techniques in deriving p–y curves for laterally loaded piles. Geotechnical and Geological Engineering **34**, No. 5, 1453-1473.

Holmen, J. K., Frodal, B. H., Hopperstad, O. S. & Børvik, T. (2017). Strength differential effect in age hardened aluminium alloys. International Journal of Plasticity, No. 99, 144-161.

Jardine, R. J., Buckley, R. M., Byrne, B., Kontoe, S., Macadam, R. & Vinck, K. (2019). The ALPACA research project to improve driven pile design in chalk. Proc. 17th European Conf. on Soil Mechanics and Geotechnical Engineering, Reykjavík, paper 0071.

Klinkvort, R. T. & Hededal, O. (2014). Effect of load eccentricity and stress level on monopile support for offshore wind turbines. Canadian Geotechnical Journal **51**, No. 9, 966-974.

Kong, D., Zhu, J., Long, Y., Zhu, B., Yang, Q., Gao, Y. & Chen, Y. (2021). Centrifuge modelling on monotonic and cyclic lateral behaviour of monopiles in kaolin clay. Géotechnique, ahead of print, DOI: 10.1680/jgeot.19.P.402

Lee, M., Bae, K. T., Lee, I. W. & Yoo, M. (2019). Cyclic p-y Curves of Monopiles in Dense Dry Sand Using Centrifuge Model Tests. Applied Sciences **9**, No. 8, 1641 (18 pages).

Li, Z. S., Blanc, M. & Thorel, L. (2020). Using FBGS to estimate the horizontal response of a monopile in a geotechnical centrifuge. International Journal of Physical Modelling in Geotechnics **20**, No. 3, 164-174.

Li, Z., Haigh, S. K. & Bolton, M. D. (2010). Centrifuge modelling of mono-pile under cyclic lateral loads. Proc. 7th Int. Conf. on Physical Modelling in Geotechnics, Zurich, Vol. 2, 965-970.

McAdam, R. A., Byrne, B. W., Houlsby, G. T., Beuckelaers, W. J. A. P., Burd, H. J., Gavin, K. G., Igoe, D. J. P., Jardine, R. J., Martin, C. M., Muir Wood, A., Potts, D. M., Skov Gretlund, J., Taborda, D. M. G. & Zdravković, L. (2020). Monotonic laterally loaded pile testing in a dense marine sand at Dunkirk. Géotechnique **70**, No.11, 986-998.

Mezazigh, S. (1995). Étude expérimentale de pieux chargés latéralement : proximité d'un talus et effet de groupe. Doctoral dissertation, École Centrale de Nantes, Nantes, France (in French).

Mitchell, J. K. (2008). Aging of sand—A continuing enigma? Proc. 6th Int. Conf. on Case Histories in Geotechnical Engineering, Arlington VA, 1–21.

Palmer, M. C., O'Rourke, T. D., Olson, N. A., Abdoun, T., Ha, D. & O'Rourke, M. J. (2009). Tactile pressure sensors for soil-structure interaction assessment. Journal of Geotechnical and Geoenvironmental Engineering **135**, No. 11, 1638-1645.

Puech, A. & Garnier, J. (2017). Design of piles under cyclic loading: SOLCYP recommendations. London: ISTE - Wiley.

Puech, A., Canou, J., Bernardini, C., Pecker, A., Jardine, R. J. & Holeyman, A. (2012). SOLCYP: a four-year joint industry project on the behaviour of piles under cyclic loading. Proc. 7th Int. Conf. on Offshore Site Investigation and Geotechnics, London, 263-270.

Rakotonindriana, J. (2009). Comportement des pieux et des groupes de pieux sous chargement latéral cyclique. Doctoral dissertation, École Centrale de Nantes, Nantes, France (in French).

Remaud, D. (1999). Pieux sous charges latérales: étude expérimentale de l'effet de groupe. Doctoral dissertation, École Centrale de Nantes, Nantes, France (in French).

Rosquoët, F. (2004). Pieux sous charge latérale cyclique. Doctoral dissertation, École Centrale de Nantes, Nantes, France (in French).

Rosquoët F., Thorel L., Garnier J., Canépa Y., (2007). Lateral cyclic loading of sand-installed piles. Soils and Foundations **47**, No. 5, 821-832.

Schmertmann, J. H. (1991). The mechanical aging of soils. Journal of Geotechnical Engineering **117**, No. 9, 1288-1330.

Shakhirev, V. & Ejjaouani, H. (1995). Étude expérimentale de pieux rigides courts soumis à des charges horizontales. Bulletin de Liaison des Laboratoires des Ponts et Chaussées, No. 196, 27-42.

Truong, P., Lehane, B. M., Zania, V. & Klinkvort, R. T. (2019). Empirical approach based on centrifuge testing for cyclic deformations of laterally loaded piles in sand. Géotechnique **69**, No. 2, 133-145.

Zhu, B., Wen, K., Li, T., Wang, L. & Kong, D. (2019). Experimental study on lateral pile–soil interaction of offshore tetrapod piled jacket foundations in sand. Canadian Geotechnical Journal **56**, No. 11, 1680-1689.

Table 1 Physical properties of Fontainebleau NE34 sand

G_s	d_{10} (mm)	d_{50} (mm)	d_{60} (mm)	C_u (=d_{60}/d_{10})	$\rho_{d\text{-}min}$ (g/cm^3)	$\rho_{d\text{-}max}$ (g/cm^3)
2.647	0.151	0.210	0.221	1.466	1.434	1.746

Table 2 Scaling up of modelling parameters to prototype ones

Parameter	Model	Prototype
D (m)	0.05	5
d (m)	0.045	4.5
E (GPa)	74	74
EI (N·m^2)	7.8×10^3	7.8×10^{11}
L (m)	0.15, 0.25, 0.35, 0.45	15, 25, 35, 45
L_e (m)	0.25, 0.50, 0.75	25, 50, 75

Captions of figures

Figure 1 Geometry of the instrumented model piles

Figure 2 Lateral loading and measuring systems: (a) schema; (b) photograph

Figure 3 Testing program: pile's (a) installation position and (b) embedment and loading eccentricity

Figure 4 Determination of pivot point with global and incremental methods

Figure 5 Sequence of data processing

Figure 6 Distributions of (a) strain and (b) differential strain for L/D = 3, 5, 7 and 9

Figure 7 Profiles of pile deflection, rotation angle, bending moment, shear force and soil reaction for L/D = (a) 3, (b) 5, (c) 7 and (d) 9

Figure 8 Normalised pivot depths determined by (a) incremental method and (b) global method for tests with constant load eccentricity (L_e/D = 10)

Figure 9 Relationship between soil reaction and normalised deflection at different depths for L/D = (a) 3, (b) 5, (c) 7 and (d) 9

Figure 10 Relationship among the ground-level bending moment, lateral load, pile deflection and rotation angle for L/D = 3, 5, 7 and 9

Figure 11 Distributions of (a) strain and (b) differential strain for L_e/D = 5, 10 and 15

Figure 12 Profiles of pile deflection, rotation angle, bending moment, shear force and soil reaction for L_e/D = (a) 5, (b) 10, and (c) 15

Figure 13 Normalised pivot depths determined by (a) incremental method and (b) global method for tests with constant embedding depth (L/D = 5)

Figure 14 Relationship between normalised deflection and soil reaction at different depths for L_e/D = (a) 5, (b) 10 and (c) 15

Figure 15 Relationship among the ground-level bending moment, lateral load, pile deflection and rotation angle for L_e/D = 5, 10 and 15

Figure 16 Schematic drawing of stress state of a laterally loaded monopile

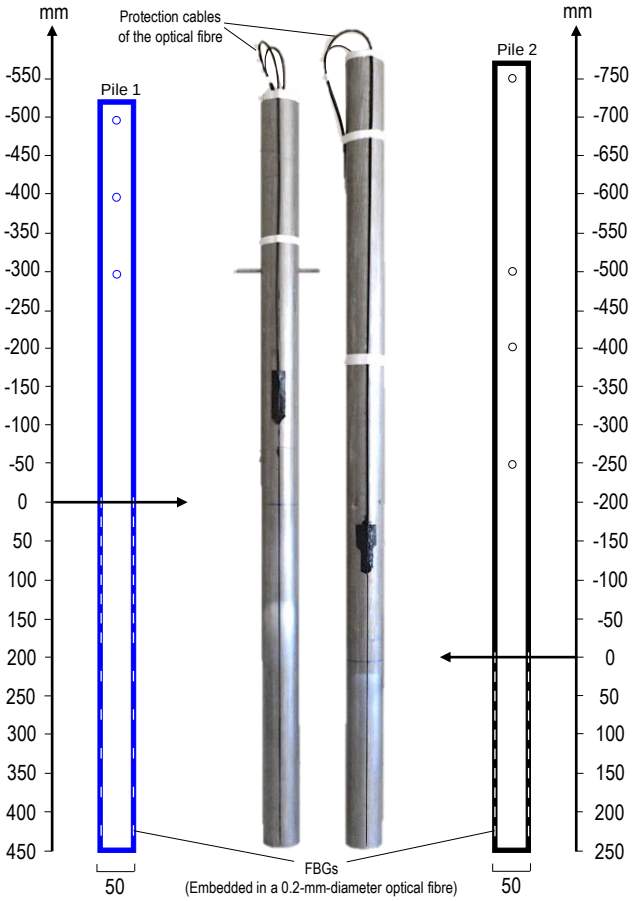
mm
Protection cables
of the optical fibre
Pile 1
Pile 2
mm
-550
-500
-450
-400
-350
-300
-250
-200
-150
-100
-50
0
50
100
150
200
250
300
350
400
450
-750
-700
-650
-600
-550
-500
-450
-400
-350
-300
-250
-200
-150
-100
-50
0
50
100
150
200
250
50
FBGs
(Embedded in a 0.2-mm-diameter optical fibre)
50

Figure 1

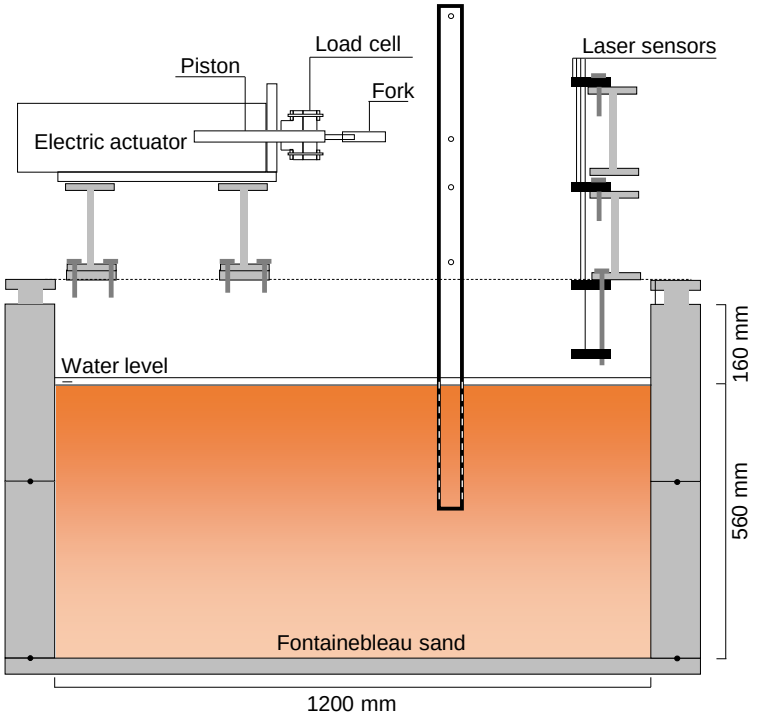
Load cell
Piston
Fork
Laser sensors
Electric actuator
Water level
160 mm
560 mm
Fontainebleau sand
1200 mm

(a)

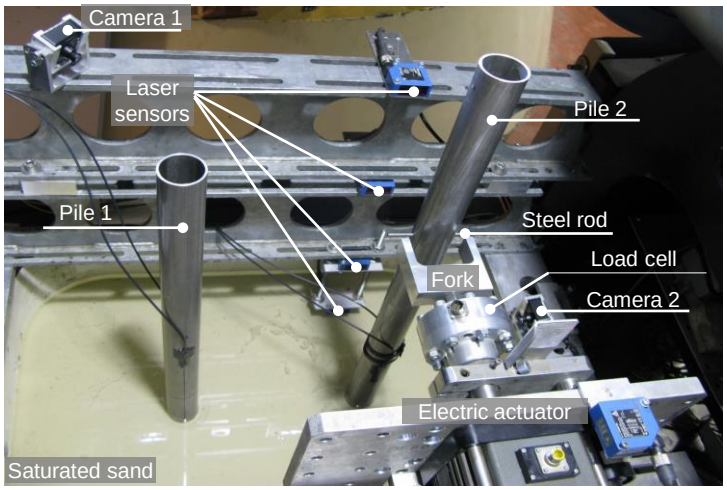
Camera 1
Laser sensors
Pile 2
Pile 1
Steel rod
Load cell
Fork
Camera 2
Electric actuator
Saturated sand

(b)

Figure 2

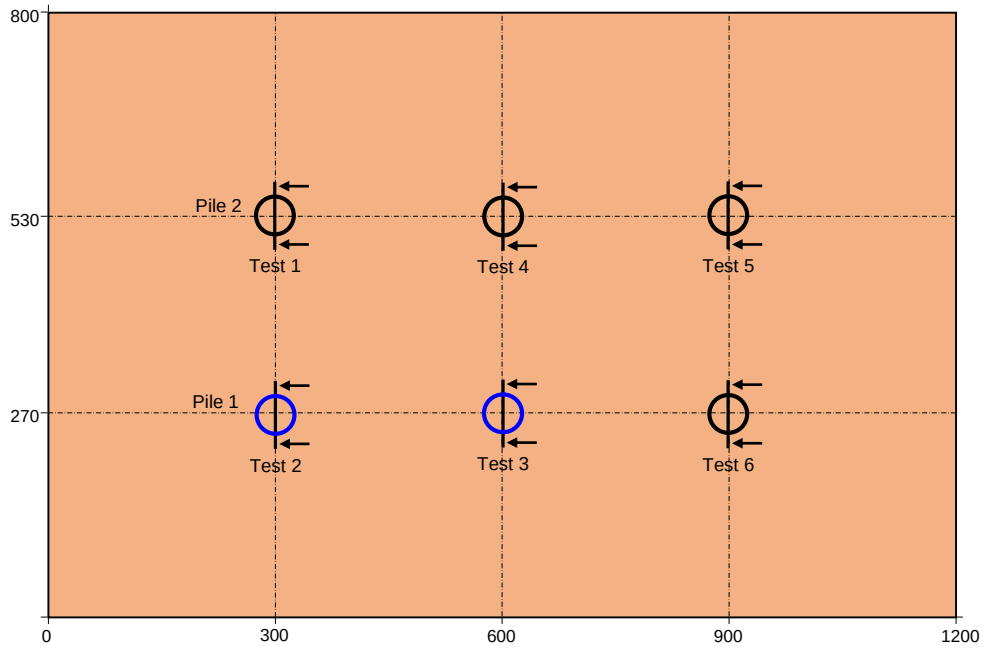
800
530
270
0
300
600
900
1200
Pile 2
Test 1
Test 4
Test 5
Pile 1
Test 2
Test 3
Test 6

(a)

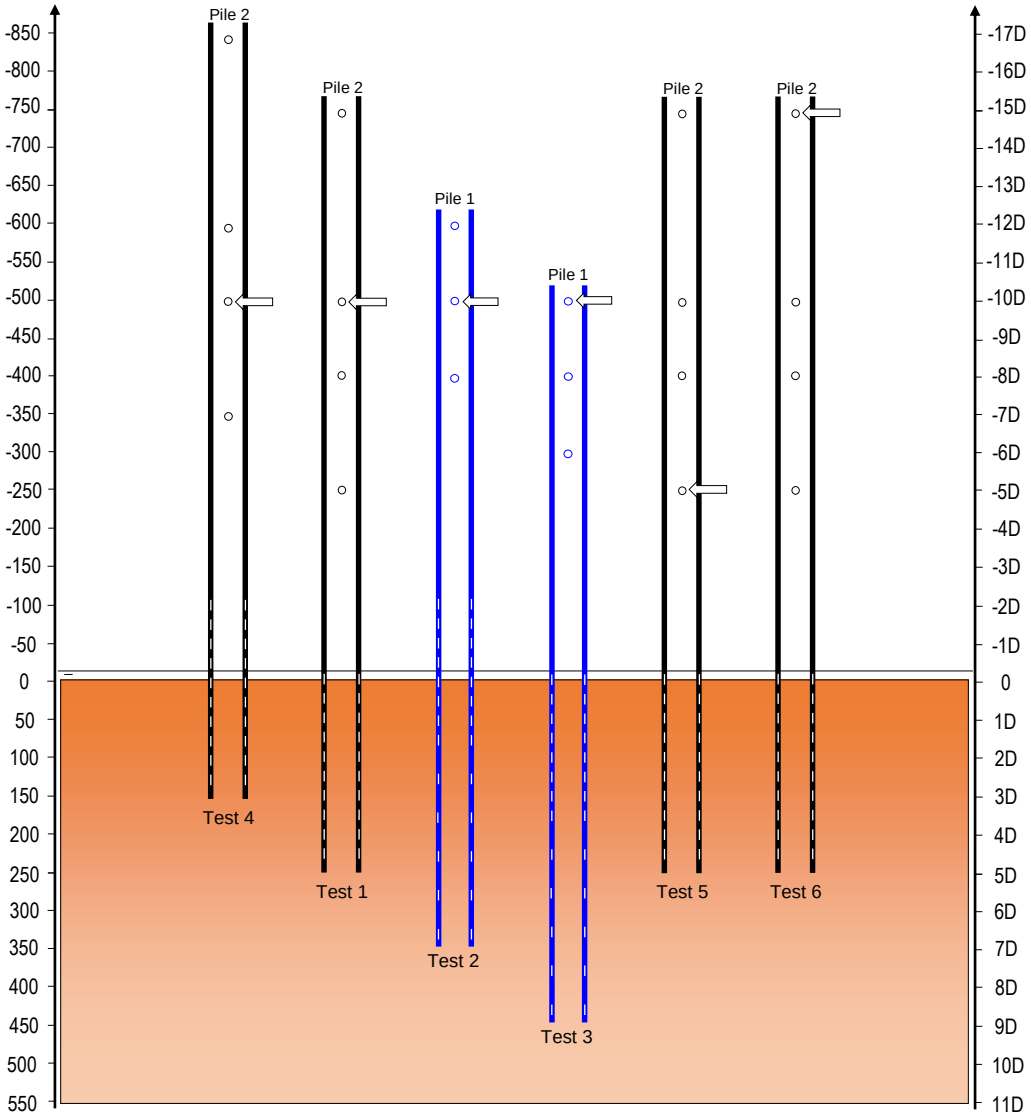
-850
-800
-750
-700
-650
-600
-550
-500
-450
-400
-350
-300
-250
-200
-150
-100
-50
0
50
100
150
200
250
300
350
400
450
500
550
-17D
-16D
-15D
-14D
-13D
-12D
-11D
-10D
-9D
-8D
-7D
-6D
-5D
-4D
-3D
-2D
-1D
0
1D
2D
3D
4D
5D
6D
7D
8D
9D
10D
11D
Pile 2
Pile 2
Pile 1
Pile 1
Pile 2
Pile 2
Test 4
Test 1
Test 2
Test 3
Test 5
Test 6

(b)

Figure 3

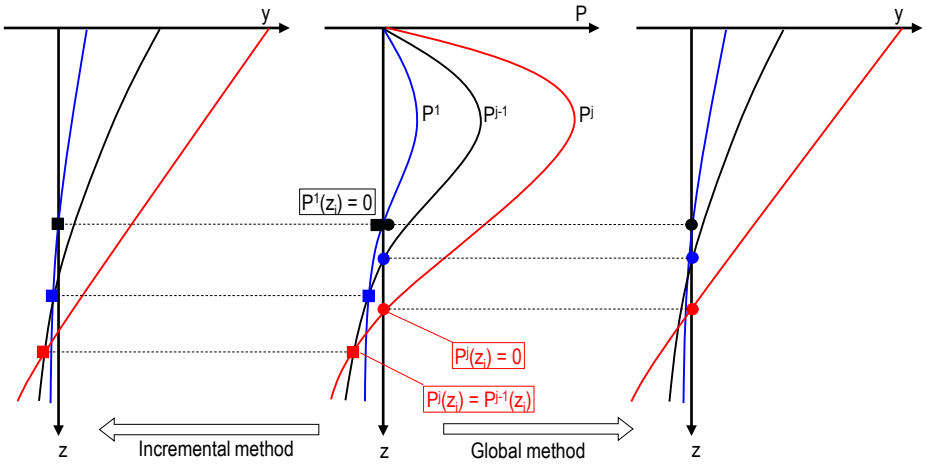
y
P
y
P1
Pj-1
Pj
P1(zi) = 0
Pi(zi) = 0
Pi(zi) = Pj-1(zi)
z
Incremental method
z
Global method
z

Figure 4

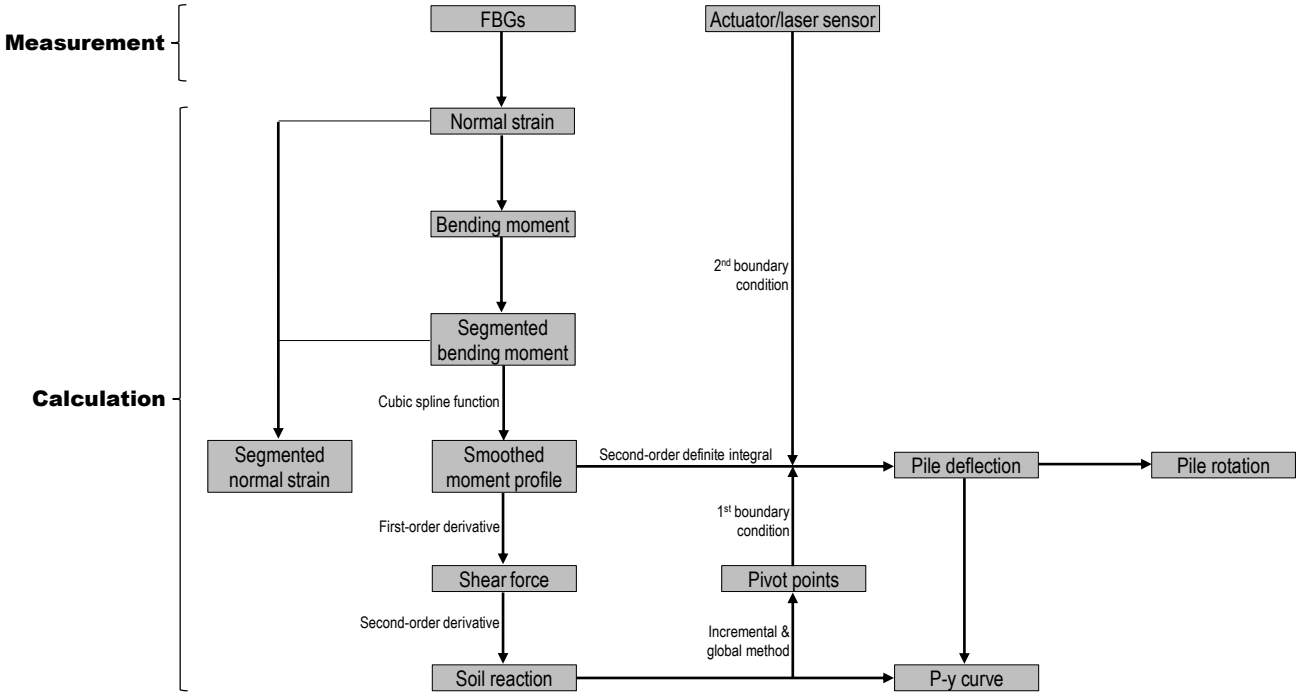
Measurement
Calculation
FBGs
Actuator/laser sensor
Normal strain
Bending moment
2nd boundary condition
Segmented bending moment
Cubic spline function
Segmented normal strain
Smoothed moment profile
Second-order definite integral
Pile deflection
Pile rotation
1st boundary condition
First-order derivative
Shear force
Pivot points
Second-order derivative
Incremental & global method
Soil reaction
P-y curve

Figure 5

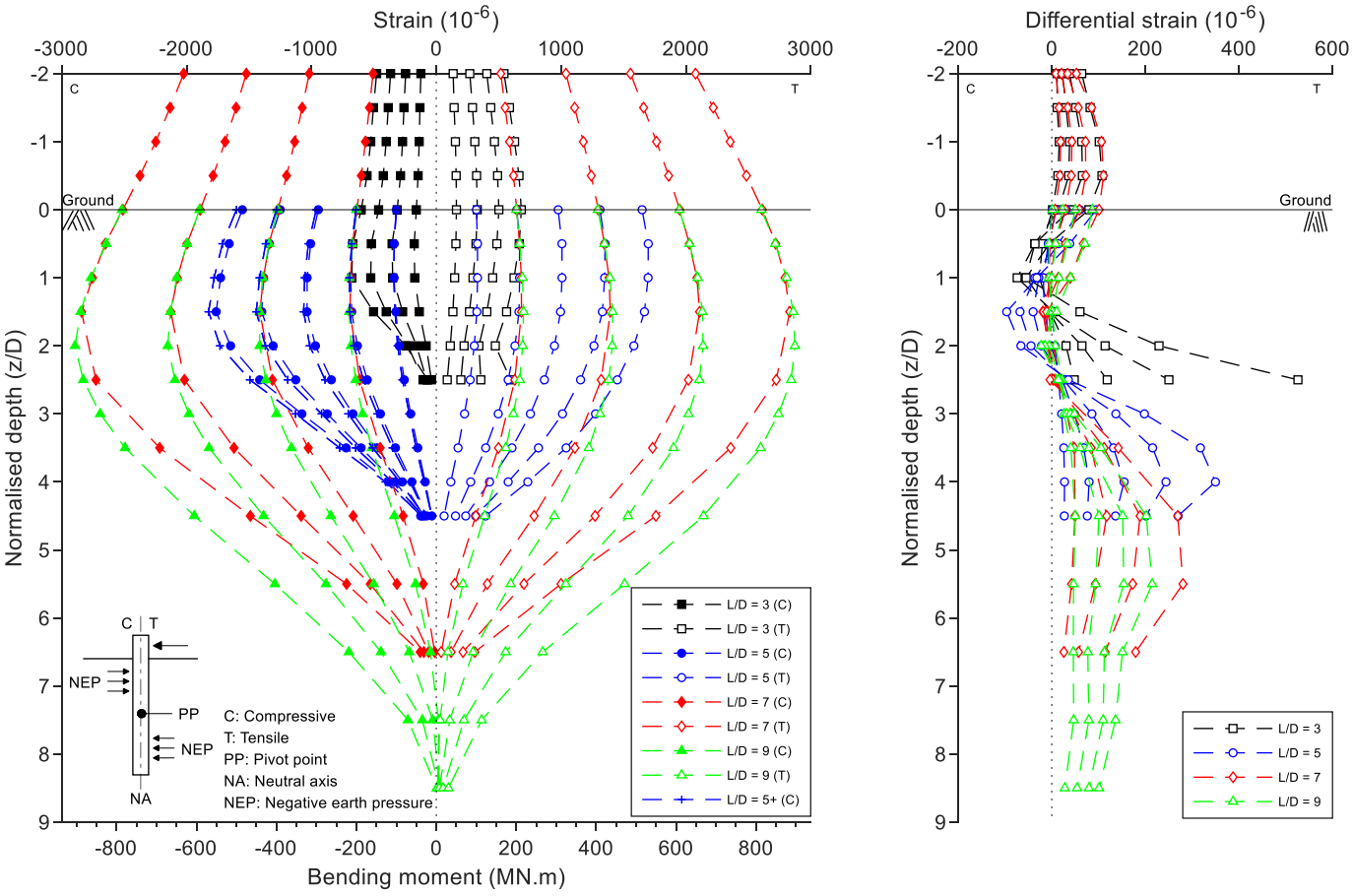
Strain (10^{-6})
-3000
-2000
-1000
0
1000
2000
3000
C
T
Ground
Normalised depth (z/D)
Bending moment (MN.m)
-800
-600
-400
-200
0
200
400
600
800
C
T
NEP
PP
NEP
NA
C: Compressive
T: Tensile
PP: Pivot point
NA: Neutral axis
NEP: Negative earth pressure
L/D = 3 (C)
L/D = 3 (T)
L/D = 5 (C)
L/D = 5 (T)
L/D = 7 (C)
L/D = 7 (T)
L/D = 9 (C)
L/D = 9 (T)
L/D = 5+ (C)
Differential strain (10^{-6})
-200
0
200
400
600
L/D = 3
L/D = 5
L/D = 7
L/D = 9

(a) (b)

Figure 6

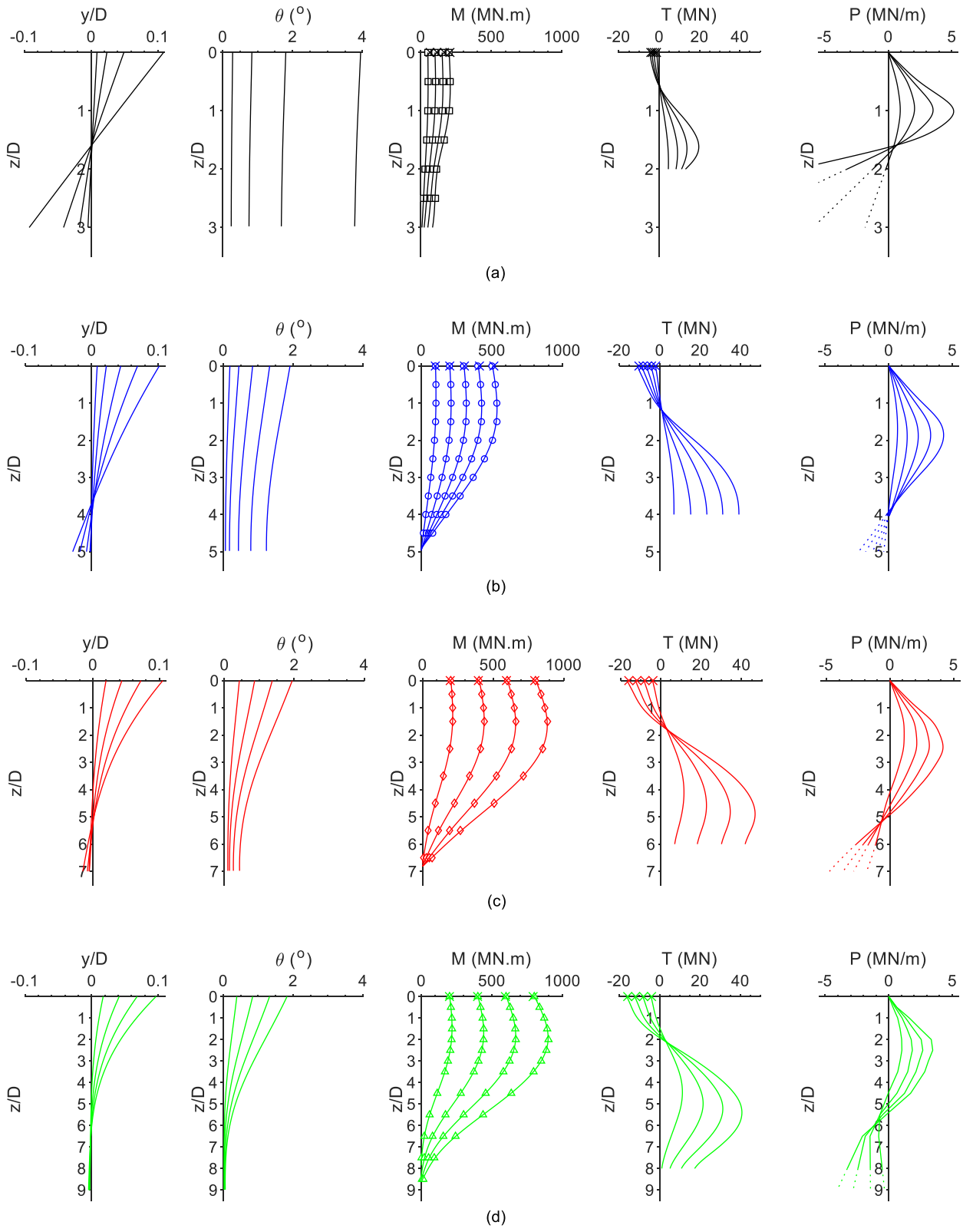

Figure 7

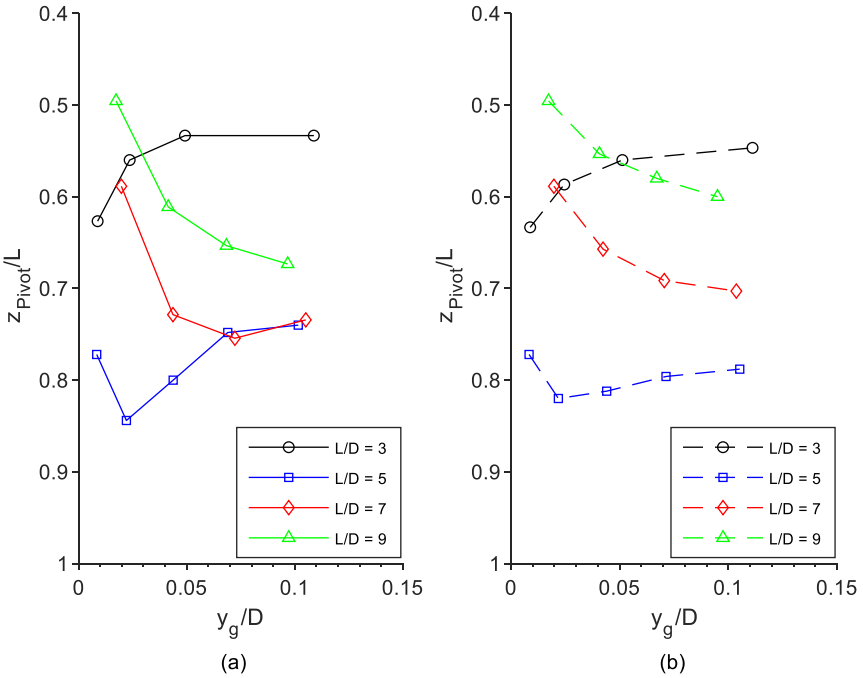

Figure 8

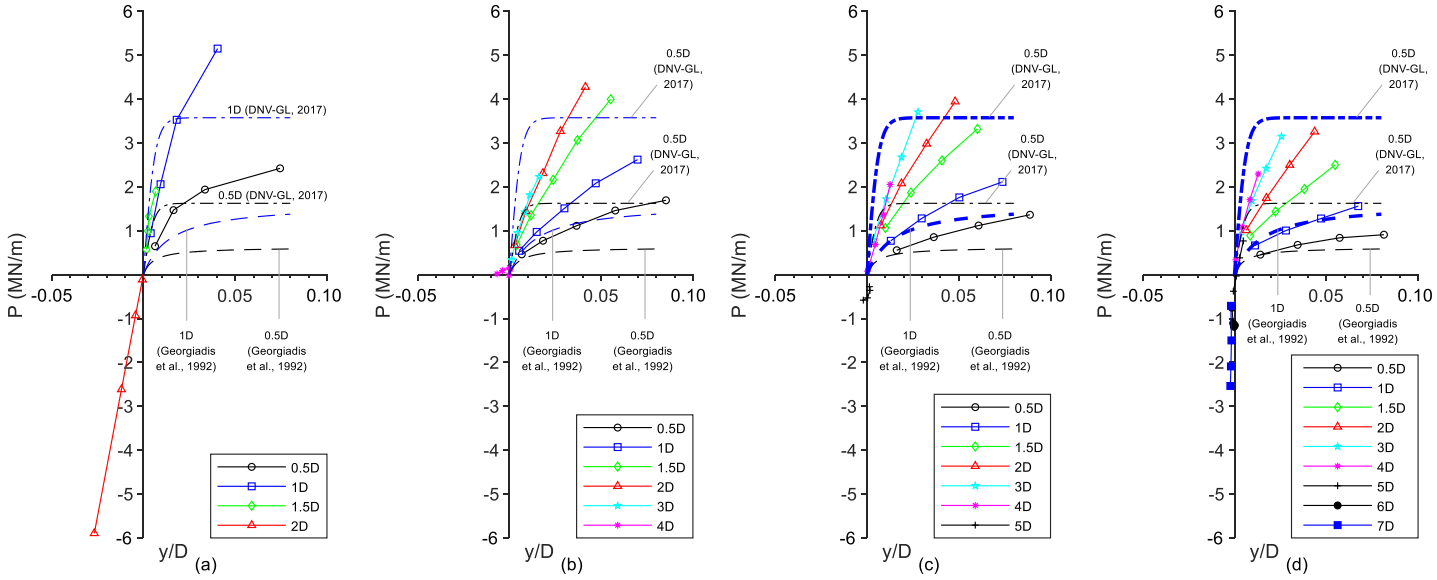
P (MN/m)
y/D
(a)
(b)
(c)
(d)
1D (DNV-GL, 2017)
0.5D (DNV-GL, 2017)
0.5D
(DNV-GL,
2017)
1D
(Georgiadis
et al., 1992)
0.5D
(Georgiadis
et al., 1992)
0.5D
1D
1.5D
2D
3D
4D
5D
6D
7D

Figure 9

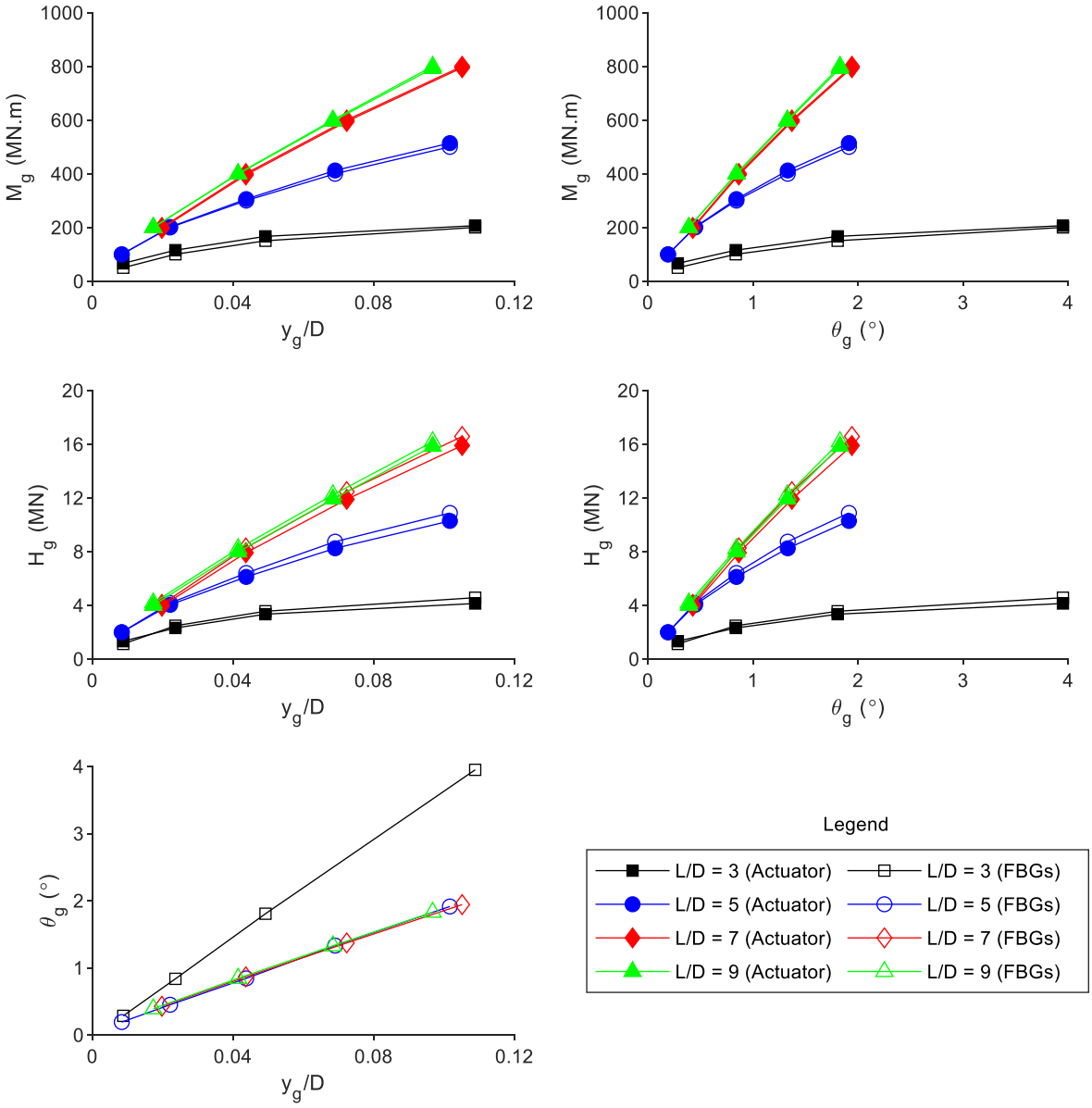
1000
800
600
400
200
0
M_g (MN.m)
0
0.04
0.08
0.12
y_g/D
θ_g (°)
1
2
3
4
20
16
12
8
4
H_g (MN)
Legend
L/D = 3 (Actuator)
L/D = 3 (FBGs)
L/D = 5 (Actuator)
L/D = 5 (FBGs)
L/D = 7 (Actuator)
L/D = 7 (FBGs)
L/D = 9 (Actuator)
L/D = 9 (FBGs)

Figure 10

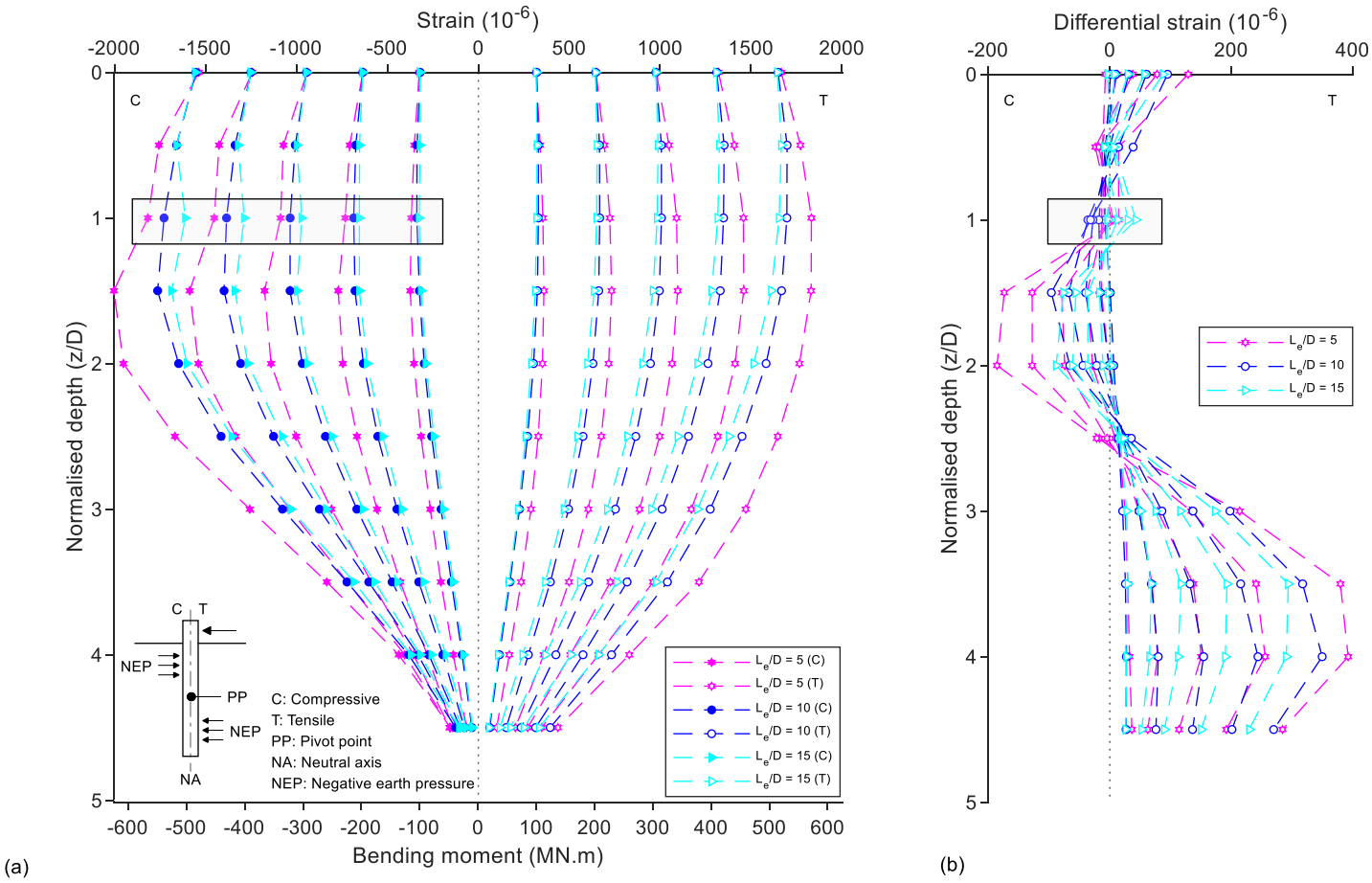
Strain (10^{-6})
Normalised depth (z/D)
Bending moment (MN.m)
C
T
NEP
PP
NA
C: Compressive
T: Tensile
PP: Pivot point
NA: Neutral axis
NEP: Negative earth pressure
L_e/D = 5 (C)
L_e/D = 5 (T)
L_e/D = 10 (C)
L_e/D = 10 (T)
L_e/D = 15 (C)
L_e/D = 15 (T)
(a)
Differential strain (10^{-6})
Normalised depth (z/D)
L_e/D = 5
L_e/D = 10
L_e/D = 15
(b)

Figure 11

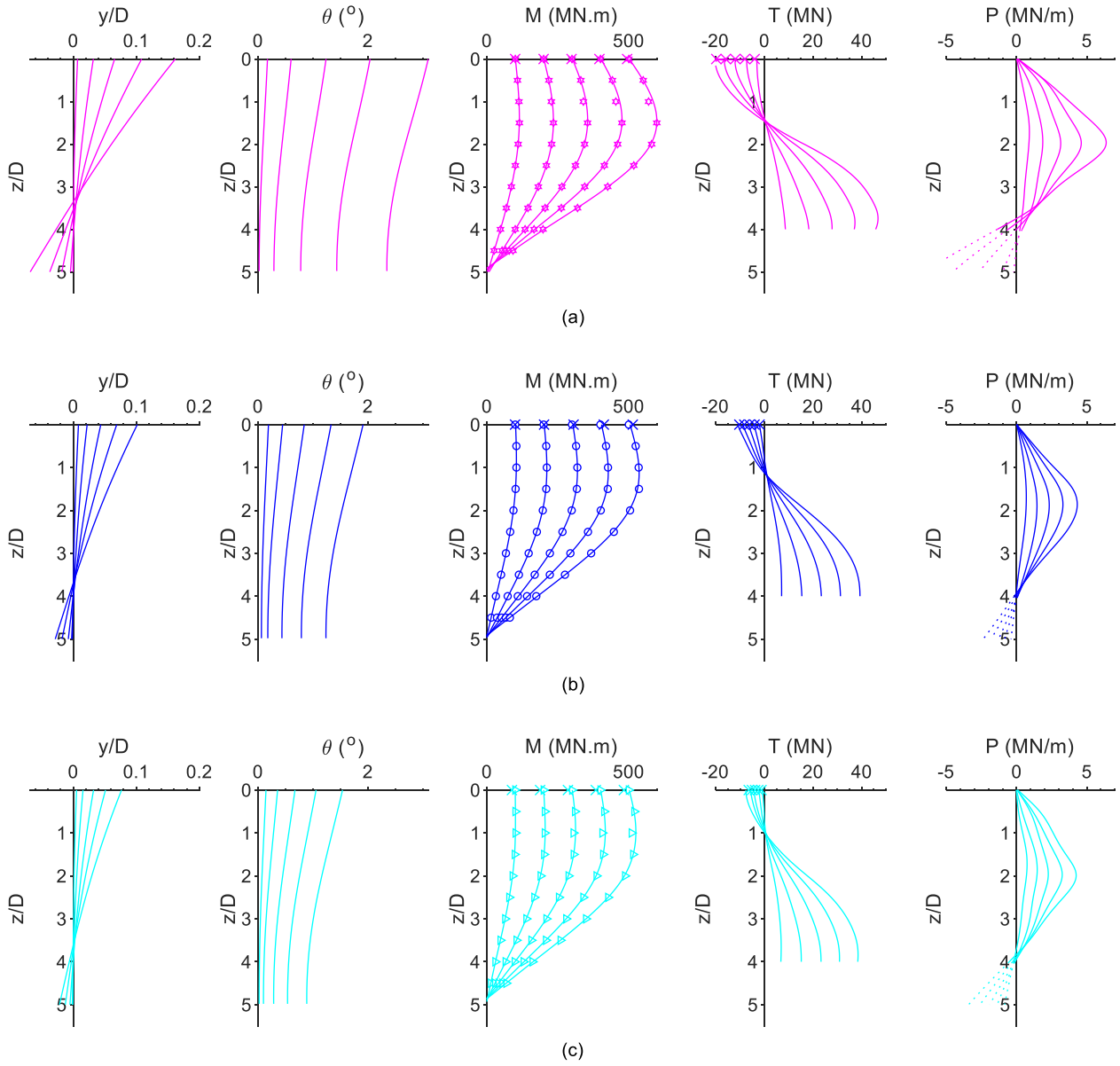

Figure 12

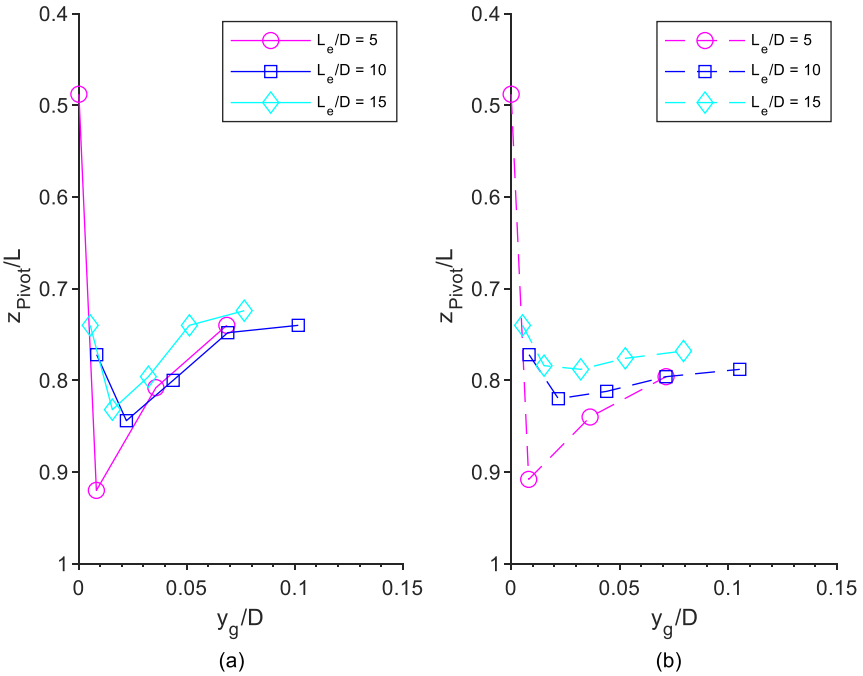

Figure 13

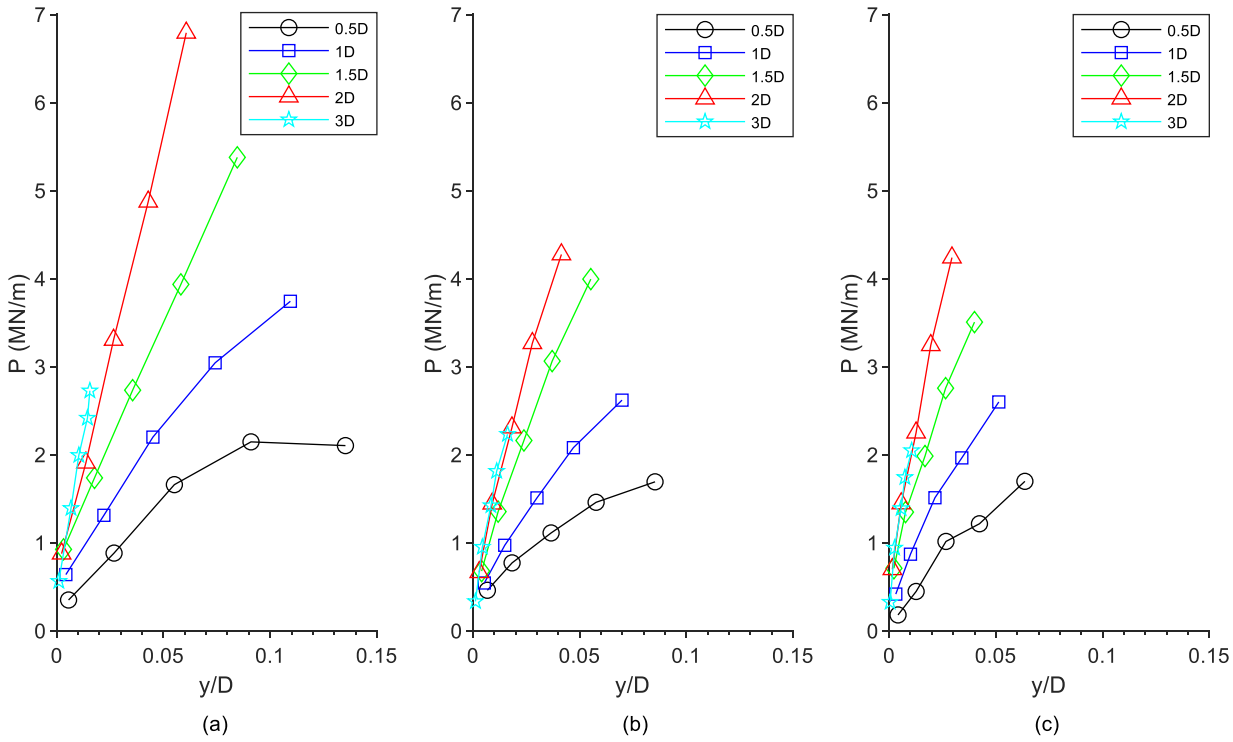

Figure 14

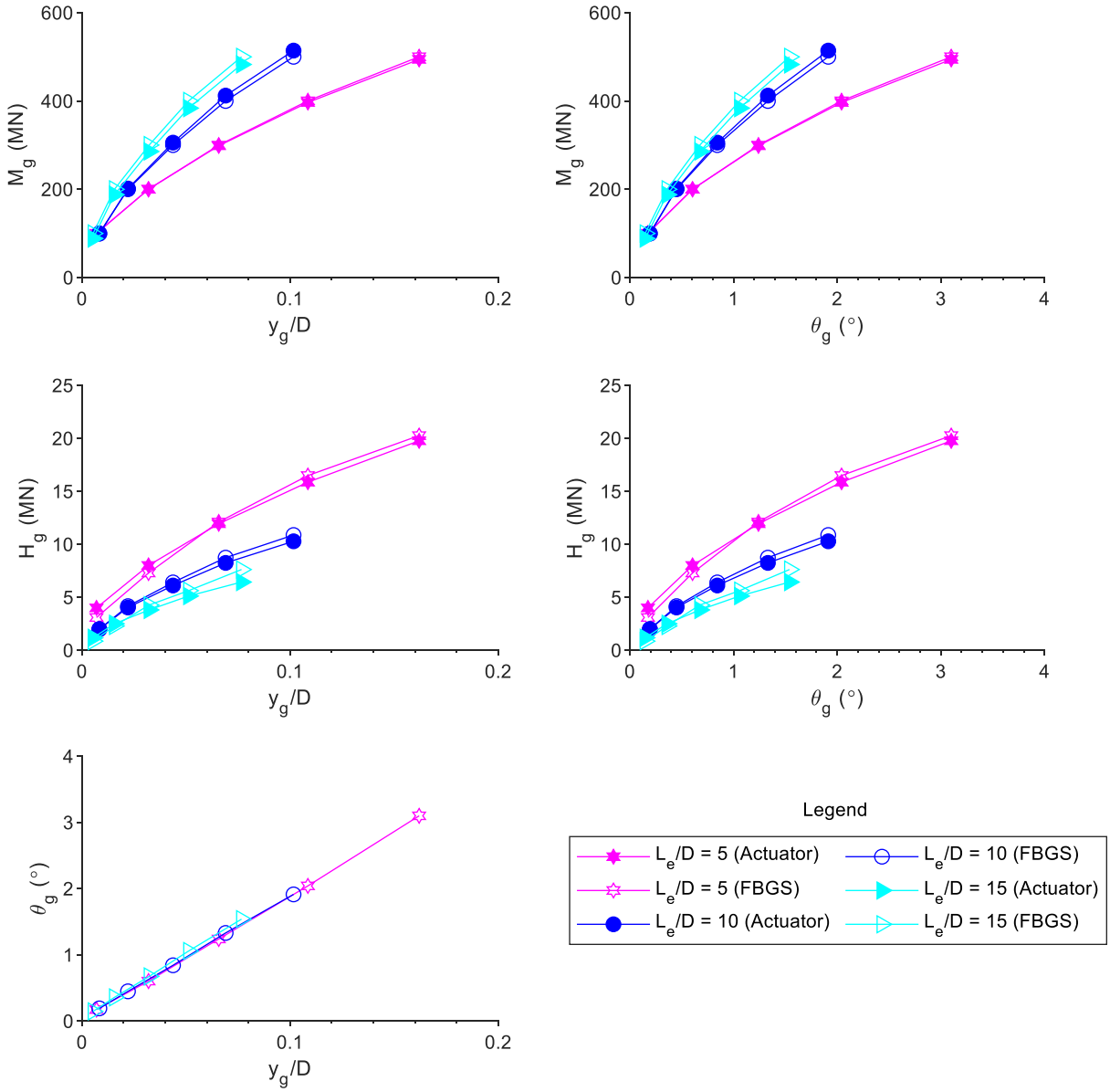
600
400
200
0
M_g (MN)
0
0.1
0.2
y_g/D
0
1
2
3
4
θ_g (°)
25
20
15
10
5
H_g (MN)
4
3
2
1
Legend
L_e/D = 5 (Actuator)
L_e/D = 5 (FBGS)
L_e/D = 10 (Actuator)
L_e/D = 10 (FBGS)
L_e/D = 15 (Actuator)
L_e/D = 15 (FBGS)

Figure 15

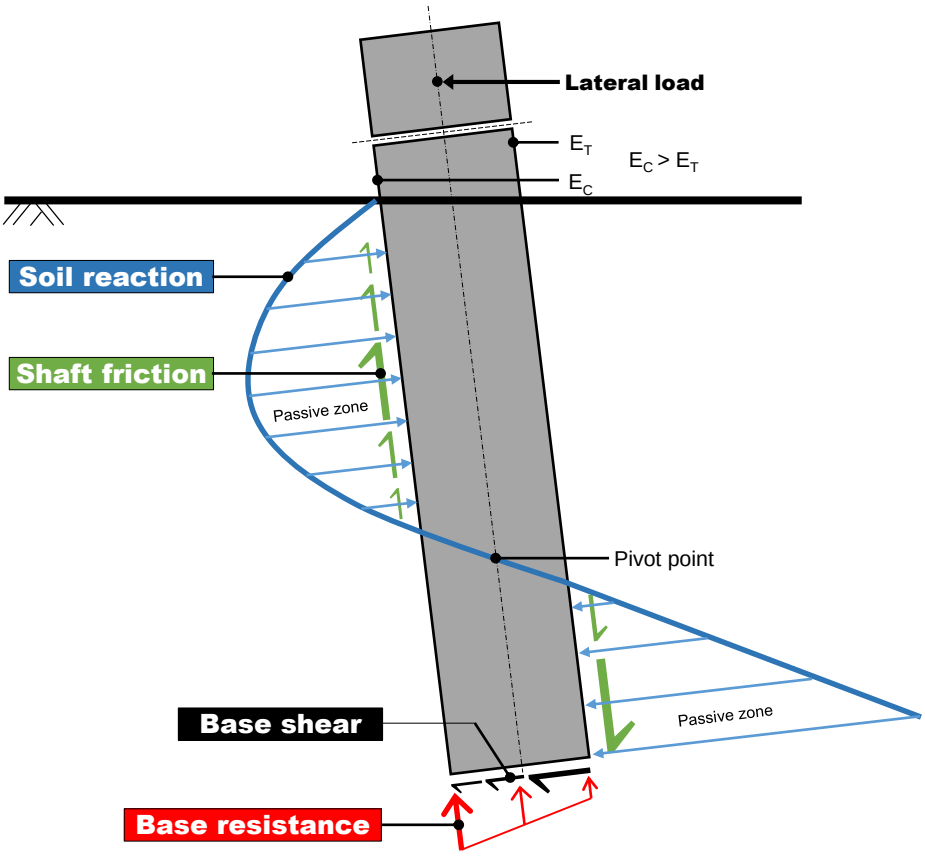
Lateral load
E_T
$E_C > E_T$
E_C
Soil reaction
Shaft friction
Passive zone
Pivot point
Base shear
Passive zone
Base resistance

Figure 16